Celestial Mechanics and Dynamical Astronomy

Averaged model to study long-term dynamics of a probe about Mercury

--Manuscript Draft--

Manuscript Number:	CELE-D-17-00054R3
Full Title:	Averaged model to study long-term dynamics of a probe about Mercury
Article Type:	Original Research
Keywords:	Frozen orbits; orbital dynamics; averaged models
Corresponding Author:	Eva Tresaco Centro Universitario de la Defensa Zaragoza Zaragoza, SPAIN
Corresponding Author Secondary Information:	
Corresponding Author's Institution:	Centro Universitario de la Defensa Zaragoza
Corresponding Author's Secondary Institution:	
First Author:	Eva Tresaco
First Author Secondary Information:	
Order of Authors:	Eva Tresaco
	Jean Paulo S. Carvalho
	Antonio Elipe
	Antonio F. B. A. Prado
	Rodolpho Vilhena de Moraes
Order of Authors Secondary Information:	
Funding Information:	Ministerio de Economía y Competitividad (ESP2013-44217-R) — Dr. Eva Tresaco
	Conselho Nacional de Desenvolvimento Científico e Tecnológico (306953/2014-5, 420674/2016-0) — Dr. Jean Paulo S. Carvalho
Abstract:	This article provides a method for finding initial conditions of frozen orbits for a probe around Mercury. Frozen orbits are those whose orbital elements remain constant on average. Thus, at a given latitude, the satellite always passes at the same altitude. This is very interesting for scientific missions that require close inspection of any celestial body. The orbital dynamics of an artificial satellite about Mercury is governed by the potential attraction of the main body. Besides the Keplerian attraction, we consider the inhomogeneities of the potential of the central body. We include secondary terms of Mercury gravity field from J2 up to J6, and the tesseral harmonics C22 that is of the same magnitude than zonal J2. In the case of science missions about Mercury, it is also important to consider third-body perturbation (Sun). Circular restricted three body problem can not be applied to Mercury-Sun system due to its non-negligible orbital eccentricity. Besides the harmonics coefficients of Mercury's gravitational potential, and the Sun gravitational perturbation, our average model also includes solar acceleration pressure. This simplified model captures the majority of the dynamics of low and high orbits about Mercury. In order to capture the dominant characteristics of the dynamics, short-period terms of the system are removed applying a double averaging technique. This algorithm is a two-fold process which firstly averages over the period of the satellite, and secondly averages with respect to the period of the third body. This simplified Hamiltonian model is introduced in the Lagrange Planetary equations. Thus, frozen orbits are characterized by a surface depending on three variables: the orbital semimajor axis, eccentricity and inclination. We find frozen orbits for an average altitude of 400 km and 1000 km, which are the predicted values for the BepiColombo mission. Finally, the paper delves into the orbital

	stability of frozen orbits and the temporal evolution of the eccentricity of these orbits.
Response to Reviewers:	Dear editor and referees, We have revised our manuscript accordingly with final reviewer's comments. We have performed all the modifications suggested: •We have corrected the typos detected in the manuscript (w by ω, language and subsequently). •Page 13: following the suggestion of one of the reviewers, we have added a new subsection title 4.1 Analysis without C22, in order to clarify the structure of Sec.4. •Page 15: we have translated the sentence “now, we move..” from below Fig. 6 to above it because Fig. 6 was computed using the values indicated in the sentence. •Page 22: and finally, we have included a sentence mentioning that Fig. 17 was computed for a large SRP value to highlight the effect of this perturbation (otherwise, with beta=0.01, the curve was very close to the one without SRP). All the main changes have been marked in bold in the revised version of the manuscript. Sincerely, Eva Tresaco

Noname manuscript No.
(will be inserted by the editor)

Averaged model to study long-term dynamics of a probe about Mercury

Eva Tresaco · Jean Paulo S. Carvalho · Antonio F. B. A. Prado · Antonio Elipe · Rodolpho Vilhena de Moraes

the date of receipt and acceptance should be inserted later

Abstract This paper provides a method for finding initial conditions of frozen orbits for a probe around Mercury. Frozen orbits are those whose orbital elements remain constant on average. Thus, at the same point in each orbit, the satellite always passes at the same altitude. This is very interesting for scientific missions that require close inspection of any celestial body. The orbital dynamics of an artificial satellite about Mercury is governed by the potential attraction of the main body. Besides the Keplerian attraction, we consider the inhomogeneities of the potential of the central body. We include secondary terms of Mercury gravity field from J_2 up to J_6, and the tesseral harmonics $\overline{C}_{22}$ that is of the same magnitude than zonal J_2. In the case of science missions about Mercury, it is also important to consider third-body perturbation (Sun). Circular restricted three body problem can not be applied to Mercury-Sun system due to its non-negligible orbital eccentricity. Besides the harmonics coefficients of Mercury's gravitational potential, and the Sun gravitational perturbation, our average model also includes solar acceleration pressure. This simplified model captures the majority of the dynamics of low and high orbits about Mercury. In order to capture the dominant characteristics of the dynamics, short-period terms of the system are removed applying a double averaging technique. This algorithm is a two-fold process which firstly averages over the period of the satellite, and secondly averages with respect to the period of the third body. This simplified Hamiltonian model is introduced in the Lagrange

E. Tresaco, A. Elipe
Centro Universitario de la Defensa, 50090, Zaragoza, Spain.
Grupo de Mecánica Espacial - IUMA. Universidad de Zaragoza, Spain.
E-mail: etresaco@unizar.es

J. P. S. Carvalho
UFRB-Centro de Ciência e Tecnologia em Energia e Sustentabilidade, Universidade Federal do Recôncavo da Bahia, 44042-280 Feira de Santana-BA, Brazil.

A. F. B. A. Prado
Division of Space Mechanics and Control, INPE, CEP 12227-010 São José dos Campos, SP, Brazil

R. Vilhena de Moraes
UNIFESP- Instituto de Ciência e Tecnologia, Universidade Federal de São Paulo, 12231-280 São José dos Campos - SP, Brazil

Planetary equations. Thus, frozen orbits are characterized by a surface depending on three variables: the orbital semimajor axis, eccentricity and inclination. We find frozen orbits for an average altitude of 400 km and 1000 km, which are the predicted values for the BepiColombo mission. Finally, the paper delves into the orbital stability of frozen orbits and the temporal evolution of the eccentricity of these orbits.

1 Introduction

The long term effects on an artificial satellite about Mercury have already been documented in the literature. It is of contemporary interest since current exploration goals plan the exploration of the planet. The first mission to Mercury was called Mariner 10, which mapped half of the planet's surface during 1974 and 1975. More recently, MESSENGER went into orbit around Mercury and completed the mapping of Mercury's surface in 2013. Finally, BepiColombo is Europe's first mission to explore the planet Mercury in unprecedented detail. BepiColombo is planned for launch in 2018 and planned to enter orbit around Mercury in 2025.

Frozen orbits are a subject of inalterable interest since these orbits allow to minimize the cost of the orbit maintenance of the spacecraft. A search for frozen orbits in the context of BepiColombo mission is presented in this work. BepiColombo is a joint mission of the European Space Agency and the Japan Aerospace Exploration Agency to the planet Mercury. The mission comprises of two satellites to be launched together: the Mercury Planetary Orbiter (MPO) and the Mercury Magnetospheric Orbiter (MMO). Perturbing forces acting on their keplerian orbits include Mercury's non-spherical mass distribution, the gravitational force of other planets and the Sun, as well as radiation pressure from direct sunlight.

The spacecraft motion about Mercury has been studied by different authors. Lara et al. (2010) [17] developed an analytical theory considering a dynamical model based on the non-sphericity of the planet (J_2 and J_3) and the gravitational effect of the third body in elliptical and planar orbit. Ma and Lie (2013) [20] proposed a continuous control method to build artificial frozen orbits around Mercury. While, Tresaco et al. (2016) [28] studied the long term dynamics around Mercury using a simplified Hamiltonian that includes J_2 and J_3 and the gravitational attraction of the Sun, as well as radiation pressure. Nevertheless, these papers took the values $J_2 = 6 \times 10^{-5}$ and $J_3 = J_2/2$ for the harmonic coefficients of Mercury's gravitational potential. This value was based on the Mariner 10 mission flybys, while the value of J_3 was not still determined (see Jehn et al. [14]). However, recent studies by Mazarico [22], Verma [30] and Stark et al. [27] give new estimation of Mercury's gravity field up to degree and order 50 using data collected by MESSENGER spacecraft after three years in orbit. Moreover, the second-degree coefficient $\overline{C}_{22}$ has to be considered since it is only 1/2 of the J_2 term. We will see that other zonal coefficients have also a special significance in the context of mission planning. In particular, J_3, J_4 and J_6 are only one order of magnitude smaller than J_2 and $\overline{C}_{22}$. On the other hand, lower-degree coefficients (>6) can be ignored because they are 3 or 4 orders of magnitude smaller. Consequently, we incorporate these new estimated values of the harmonic coefficients in order to present a much more realistic dynamical system, and to reveal differences with previous studies.

Besides, in addition to Mercury's gravitational forces, other forces included in our disturbing function are: gravitational attraction of the Sun and the radiation pressure from direct sunlight. We consider the acceleration due to solar radiation pressure without shadowing effect. This inverse square radial thrust applies to different forms of spacecraft propulsion, such as solar sails [11], [23] and mini-magnetospheric plasma propulsion (M2P2) [32]. Both systems use the solar wind as a free energy source. M2P2 system inflates a large magnetic bubble around the spacecraft that enable to attain unprecedented speeds. It will be very useful for exploration of the solar system and beyond. On the other hand, solar sails are very promising for the scientific community. This technology opens new and challenging possibilities to space-science missions such as deep-space exploration, space debris removal strategies and long term missions in the solar system. Recent projects consider these technological developments in mission-designing. For instance, in Paul et al. [10] it is developed a configuration for a solar sail in a low Earth orbit that allows operation in high-inclination orbits. Another example is a small space probe from NASA, propelled by a solar sail, that is bound for an asteroid; this mission is planned to be launched in 2018. Let us also mention the ambitious project supported by Prof. Hawking that will send thousand of mini-solar sails into the Earth's orbit.

Summarizing, along this paper we analyse the orbital motion of a spacecraft for an orbit altitude range from 400 km to 12000 km, which correspond to the limit values provided for BepiColombo spacecraft. Our work has been conducted in the frame of the double-averaging techniques of the disturbing function (see Broucke [3], Carvalho et al. [4] and references therein). After removing the short–periodic terms from the perturbing function of the Hill problem, the Lagrange planetary equations capture the dominant characteristics of the dynamics. The solution of the system that gives the variations of the eccentricity and argument of pericenter $\dot{\omega} = 0, \dot{e} = 0$, provides us the values of the equilibria of the reduced system. These equilibria are orbits with constant mean eccentricity and mean argument of pericenter, which are known as frozen orbits. These particular solutions may provide useful information of the long term dynamics and may be of interest in astrodynamics applications.

2 Dynamical model

Let $Oxyz$ be a Mercury-centred inertial coordinate frame. The Oxy plane coincides with the planet's equator, the x-axis is defined by the intersection line of the equatorial plane of the main body and the orbital plane of the third body: the Sun. The spacecraft orbits about the central body with semimajor axis a, eccentricity e, inclination i, right ascension of the ascending node Ω, argument of the pericenter ω, true anomaly f and mean motion n. It is assumed that the third body follows an elliptic inclined orbit around the main body with semimajor axis $a_\odot$, eccentricity $e_\odot$ and inclination $i_\odot$.

Mercury rotates on its spin axis three times for every two revolutions around the Sun with rotational rate $\gamma_M \approx 6.14$ degrees per day. It follows a highly eccentric orbit, its eccentricity is 0.206. Mercury's orbit is inclined by 7 degrees to the ecliptic (the plane of Earth's orbit), while Mercury's axial tilt is almost zero, with the best measured value as low as 2.11 ± 0.1 arcmin (0.034 degrees). This measured obliquity

provided observational evidence that Mercury is very near a Cassini state (Margot et al [21]), in which its spin vector is nearly perpendicular to the orbital plane and precesses at the same rate as the orbital plane. Hence, as we define the equatorial plane as the reference plane, the orbit inclination of the third body is set to 0.034 degrees (see Fig. 1 and Table 1).

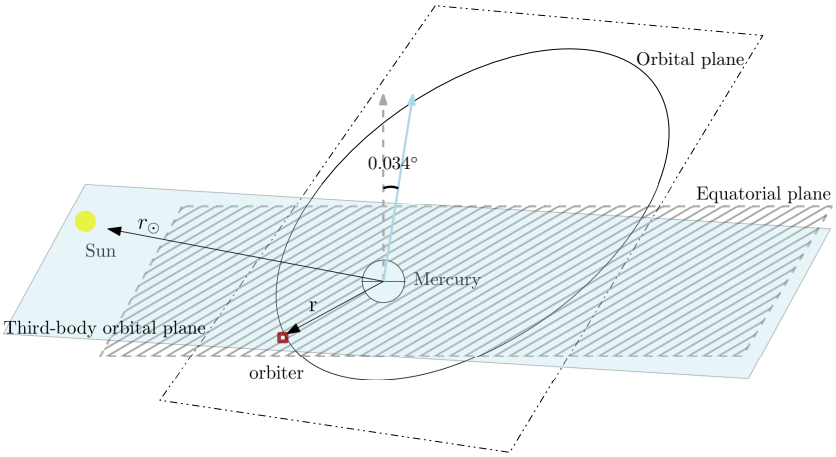

Fig. 1 Scheme of the dynamical system.

$\mu_\odot = 132712442099\,\mathrm{km}^3/\mathrm{s}^2$	$a_\odot = 5.79 \times 10^7 \mathrm{km}$	$e_\odot = 0.206$	$i_\odot = 0.034\,^\circ$	$\gamma_M = 6.14\,^\circ/\mathrm{day}$

Table 1 Orbital parameters (symbol $_\odot$ means relative to Mercury's orbit around the Sun).

Further exploration of planet Mercury have improved the knowledge of its gravity field. The major and most recent parameters of gravity field solution, termed HgMUCLA40x40, were obtained from the tracking of MESSENGER during its three years in orbit. They are listed in Table 2.

μ ($\mathrm{km}^3/\mathrm{s}^2$)	22032.09	Equatorial radius (km)	2439.7
$\overline{C}_{20}$	-2.25100×10^{-5}	$\overline{C}_{22}$	1.24973×10^{-5}
$\overline{C}_{30}$	-4.71444×10^{-6}	$\overline{C}_{40}$	-5.89291×10^{-6}
$\overline{C}_{50}$	2.98686×10^{-7}	$\overline{C}_{60}$	1.90218×10^{-6}

Table 2 Mercury's bulk parameters and normalized harmonics coefficients (HgMUCLA40x40, Verma 2016 [30]).

We consider the motion of a spacecraft around Mercury. Therefore, the main perturbations that must be considered are the following:

– Sun gravitational perturbation
– Solar radiation pressure, and

– Mercury non-sphericity effects.

Hence, the trajectory will be perturbed by the anomalies in the gravity field of Mercury: the low level gravitational field ($\overline{C}_{20}$, $\overline{C}_{22}$, $\overline{C}_{30}$, $\overline{C}_{40}$, $\overline{C}_{50}$, $\overline{C}_{60}$), the Sun's gravity attraction and the direct radiation pressure of the Sun. As we want analytic solutions, the Hamiltonian function has to be as simple as possible, yet capable to account accurately for the orbital behaviour of real satellites. Let us derive the equations of motion, and then, compute the accelerations caused by each disturbing effect to check the validity of the model proposed.

The equation of motion of the spacecraft is given by

$$\ddot{\mathbf{r}} = \ddot{\mathbf{r}}_M + \ddot{\mathbf{r}}_{3b} + \ddot{\mathbf{r}}_{SRP}, \tag{1}$$

where $\ddot{\mathbf{r}}_M$ is the force induced by Mercury gravity field (Eq. 2), $\ddot{\mathbf{r}}_{3b}$ is the resultant of the gravitational attraction of the Sun (Eq. 7), and $\ddot{\mathbf{r}}_{SRP}$ is the effect of direct solar radiation pressure (Eq. 10).

2.1 Mercury's gravity attraction

The force induced by Mercury gravity field can be expressed as the gradient of a certain potential U_M. It is written in terms of the position vector $\mathbf{r}$ of the spacecraft with respect to the central planet Mercury,

$$\ddot{\mathbf{r}}_M = \nabla U_M(\mathbf{r}). \tag{2}$$

We take into account the disturbing potential due to the non-uniform distribution of mass of Mercury. The gravitational potential U_M, expressed in the rotating reference frame, is in terms of a double infinite series of spherical harmonics dependent on latitude and longitude (see e.g. Battin [2])

$$\mathbf{U_M} = \frac{\mu}{r} + \frac{\mu}{r}\sum_{n=2}^{\infty}\sum_{j=0}^{n}\left(\frac{R_M}{r}\right)^n \overline{P}_{n,j}(\sin\phi)\Big(\overline{C}_{n,j}\cos(j\lambda) + \overline{S}_{n,j}\sin(j\lambda)\Big), \tag{3}$$

where r is the distance from the spacecraft to Mercury: $r = \|\mathbf{r}\|$, μ is the standard gravitational parameter, R_M is the equatorial radius of the planet and γ_M the rotation velocity of Mercury around its axis (see Table 1). On the other hand, (λ, ϕ) are the planetographic coordinates of the spacecraft, $\overline{P}_{n,j}$ are the normalized associated Legendre polynomials of degree n and order j. $\overline{C}_{n,j}$ and $\overline{S}_{n,j}$ are the normalized dimensionless spherical harmonic coefficients [15].

Zero order terms are independent of longitude: the zonal harmonics $J_n = -\overline{C}_{n,0}$. The even zonal harmonics are symmetric about the equator. The odd zonal harmonics are antisymmetric about the equator and define the pear-shape asymmetry of the planet. Tesseral harmonics depend on longitude; in particular $\overline{C}_{22}$ represents the polar and equatorial flattening (see Fig. 2). According to the data provided by MESSENGER mission, shown in Table 2, we consider zonal terms up to the sixth order. Following these data, we observe that the coefficient of second degree and order $\overline{C}_{22}$ plays a key role in Mercury gravity field, so we include it in our disturbing function. Note that Mercury's $\overline{C}_{22}$ is so significant with respect to the one of the Earth due to the rotation rate. The Earth spins much faster than it orbits, this fact tends to circularize its equatorial section. However, Mercury is

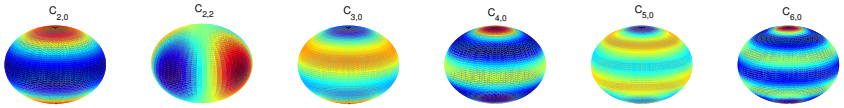

Fig. 2 Types of spherical harmonics considered in the dynamical model.

locked into a 3:2 spin-orbit resonance, which favours the tidal deformation of the planet and results in a significant triaxiality (see Noyelles et al. [26]).

Subsequently, and using the definition of the Legendre polynomials for the zonal terms up to sixth degree and spherical trigonometry: $\sin\phi = \sin i \sin(\omega + f)$, we get that the perturbation due to the zonal terms, denoted by R_{J_n}, is given by

$$
\begin{aligned}
R_{J_2} &= -\frac{1}{2} J_2 R_M^2 \frac{a^3 n^2}{r^3} \left(3{s_i}^2 \sin^2(\omega + f) - 1\right), \\
R_{J_3} &= -\frac{1}{2} J_3 R_M^3 \frac{a^4}{r^4} \frac{n^2}{a} (5{s_i}^3 \sin^3(\omega + f) - 3 s_i \sin(f + \omega)), \\
R_{J_4} &= -\frac{1}{8} J_4 R_M^4 \frac{a^5}{r^5} \frac{n^2}{a^2} \left(35{s_i}^4 \sin^4(\omega + f) - 30{s_i}^2 \sin^2(\omega + f) + 3\right), \\
R_{J_5} &= -\frac{1}{8} J_5 R_M^5 \frac{a^6}{r^6} \frac{n^2}{a^3} \left(63{s_i}^5 \sin^5(f + \omega) - 70{s_i}^3 \sin^3(\omega + f) + 15 s_i \sin(f + \omega)\right), \\
R_{J_6} &= -\frac{1}{16} J_6 R_M^6 \frac{a^7}{r^7} \frac{n^2}{a^4} \left(231{s_i}^6 \sin^6(\omega + f) - 315{s_i}^4 \sin^4(\omega + f) + 105{s_i}^2 \sin^2(f + \omega) - 5\right),
\end{aligned}
\tag{4}
$$

where $s_i = \sin i$ and $c_i = \cos i$.

On the other hand, the Legendre polynomial for the tesseral $\overline{C}_{22}$ term can be written in the following form (details can be found in Giacaglia [12] and Celletti et al. [6]),

$$
\overline{P}_{2,2}(\sin\phi)\cos 2\lambda = 6\left(\xi^2 \cos^2 f + \chi^2 \sin^2 f + \xi\chi \sin 2f) - 3(1 - s_i^2 \sin^2(f + \omega)\right),
\tag{5}
$$

where we denote $\xi = \cos\omega\cos\Omega - c_i \sin\omega \sin\Omega$ and $\chi = -\sin\omega\cos\Omega - c_i \cos\omega\sin\Omega$. After some trigonometric manipulations we get that the perturbation due to $\overline{C}_{22}$ term, denoted by $R_{C_{22}}$, is given by

$$
R_{C_{22}} = \frac{a^3}{r^3} \overline{C}_{22} R_M^2 n^2 \Big(6\xi^2 \cos^2 f + 6\chi^2 \sin f^2 + 12\xi\chi \sin(2f) - 3 + 3{s_i}^2 \sin^2(\omega + f)\Big).
\tag{6}
$$

2.2 Third body attraction

The term $\ddot{\mathbf{r}}_{3b}$ is the resultant of the gravitational attraction of the Sun. It is formulated using the third body perturbation in the inertial frame $Oxyz$ centred on Mercury (see e.g. Danby [7])

$$
\ddot{\mathbf{r}}_{3b} = -\mu_\odot \left(\frac{\mathbf{r} - \mathbf{r}_\odot}{\|\mathbf{r} - \mathbf{r}_\odot\|^3} + \frac{\mathbf{r}_\odot}{\|\mathbf{r}_\odot\|^3}\right),
\tag{7}
$$

where $\mu_\odot$ represents the standard gravitational parameter of the Sun (Table 1), and $\mathbf{r}_\odot$ is the position vector of the Sun with respect to Mercury. We perform the

expansion as a series of Legendre polynomials up to second order (due to the fact that every term of the expansion is bounded by $r^2(r/r_\odot)^{n-2}$ and $r \ll r_\odot$). Thus, only $n \leq 2$ terms of the direct perturbation remain (details can be found in [1], [28]). Hence, after replacing the expressions of the Legendre polynomials, we get

$$U_{3b} = \frac{\mu_\odot}{r_\odot} + \frac{\mu_\odot}{2r_\odot}\left(\frac{r}{r_\odot}\right)^2 (3\cos\psi - 1), \tag{8}$$

where ψ is the angle between radius vectors $\mathbf{r}$ and $\mathbf{r}_\odot$ After some algebraic manipulations, the disturbing function due to the third body perturbation (Broucke [3]), named R_{3b}, is

$$R_{3b} = \frac{\mu_\odot}{2r_\odot}\left(\frac{r}{r_\odot}\right)^2 \big(3(\alpha\cos f + \gamma\sin f)^2 - 1\big), \tag{9}$$

where coefficients α and γ depend on the orbital elements of the spacecraft and the third body (Appendix 6.1).

2.3 Solar radiation pressure

We account for the effect of direct solar radiation pressure (SRP) on a spacecraft. Radiation pressure is a non-gravitational force constantly acting on the spacecraft in anti-solar direction. The acceleration exerted on a perfectly reflecting body by solar radiation, expressed in the inertial frame $Oxyz$ centred on Mercury, is

$$\ddot{\mathbf{r}}_{SRP} = -2\,P\,\frac{A}{m}\,\frac{\mathbf{r} - \mathbf{r}_\odot}{\|\mathbf{r} - \mathbf{r}_\odot\|}, \tag{10}$$

where $(\mathbf{r} - \mathbf{r}_\odot)$ is the vector in the direction from the spacecraft to the Sun and A/m is the area-to-mass coefficient of the spacecraft. Note that the area referred to in the expression A/m is the cross-sectional area of the illuminated object i.e. the area that intercepts the radiation. For a non-spherical satellite, the area is a function of the orientation of the body with respect to the Sun. In this work we assume a cross-sectional area with fixed orientation perpendicular to the direction of solar radiation. The minus sign in Eq. (10) arises because the positive direction of this vector is defined oppositely to that of the acceleration. Finally, P indicates the solar radiation pressure. It is given by $P = I/c$, where I is the solar flux at the illuminated plane surface and c is the speed of light. The solar flux I is defined as the amount of energy received at the surface of the illuminated satellite. Solar constant at 1 astronomical unit (AU) is found to be 1358 W/m^2.
Let us now consider the critical loading parameter $\sigma^* = 2\,P/\mu_\odot$ (McInnes [23]), which is 1.53g/m^2 for the Earth. Nonetheless, the solar flux varies inversely with the square of the distance to the Sun. Therefore, the solar flux at Mercury is increased. It is given by

$$I = I_0\left(\frac{1}{\rho}\right)^2,$$

where I_0 is the solar constant at 1 AU and ρ is Mercury's average distance to Sun: 0.387 AU. In consequence, the critical loading parameter for Mercury is rescaled

accordingly: $\sigma^* = 1.53(1/\rho)^2 = 10.26\,\mathrm{g/m^2}$. That means that, for a spacecraft orbiting Mercury, the characteristic acceleration due to solar pressure, $a_c = 2\,P\,A/m$, is 10 times greater than for the same satellite orbiting the Earth.

Finally, we introduce the parameter $\sigma = \dfrac{m}{A}$ and $\beta = \dfrac{\sigma^*}{\sigma}$ (McInnes [23]). Thus, the disturbing function due to solar radiation pressure can be written in terms of β, a dimensionless parameter directly related to A/m,

$$U_{SRP} = -\frac{\beta\mu_\odot}{\|\mathbf{r} - \mathbf{r}_\odot\|}. \tag{11}$$

Based on the procedure followed for the third body perturbation, this function can be also expanded in terms of Legendre polynomials up to the second order, obtaining

$$R_{SRP} = -\beta\left(\mu_\odot\,\frac{r}{r_\odot^2}\cos\psi - \frac{\mu_\odot}{2\,r_\odot}\left(\frac{r}{r_\odot}\right)^2\left(3(\alpha\cos f + \gamma\sin f)^2 - 1\right)\right). \tag{12}$$

It is of interest to examine the range of variation in the ratio (A/m) encountered in practice. A useful estimation of A/m values for some satellites can be obtained from Table 3. Probably, inflatable magnetic balloons or solar sails represent the largest coefficients (see Winglee [32] and references therein). Note that the coefficients β and a_c are calculated assuming that the satellites orbit Mercury.

Satellite name	Dimensions ($\mathrm{m^2}$)	Weight (kg)	A/m ($\mathrm{m^2/kg}$)	β	a_c ($\mathrm{km/s^2}$)
BepiColombo MMO	1.9×1.1	288	$7.2 \cdot 10^{-3}$	$7.4 \cdot 10^{-5}$	$4.4 \cdot 10^{-10}$
Mariner 10	1×8	503	$1.2 \cdot 10^{-2}$	$1.6 \cdot 10^{-4}$	$7.3 \cdot 10^{-10}$
Ikaros sail	14×10	310	0.45	$4.6 \cdot 10^{-3}$	$2.7 \cdot 10^{-8}$
Sunjammer sail	34×34	30	38.5	0.39	$2.6 \cdot 10^{-6}$

Table 3 Approximate values of A/m and β coefficients for a selection of spacecrafts.

2.4 Disturbing accelerations

To facilitate the discussion of the results, we summarize the processes by which the disturbing functions described above alter the orbit of a satellite.

First of all, Figure 3 depicts the magnitude of the accelerations ($\mathrm{km/s^2}$) acting on a spacecraft as functions of the distance from the center of Mercury (km).

It is observed that the main perturbations are caused by the non-sphericity of the planet and the Sun attraction. The gravity field perturbations are obviously stronger for satellites with low orbit. Nevertheless, solar radiation pressure may be negligible when compared with the two other perturbations, or depending of the area-to-mass ratio, may even exceed the low degree and order gravitational acceleration at some orbit altitude.

The worse consequence of perturbations would be the influence in the argument of pericenter and the eccentricity. It means that the pericenter altitude may rapidly fall down and the spacecraft would end up by collision onto the planet. The increase

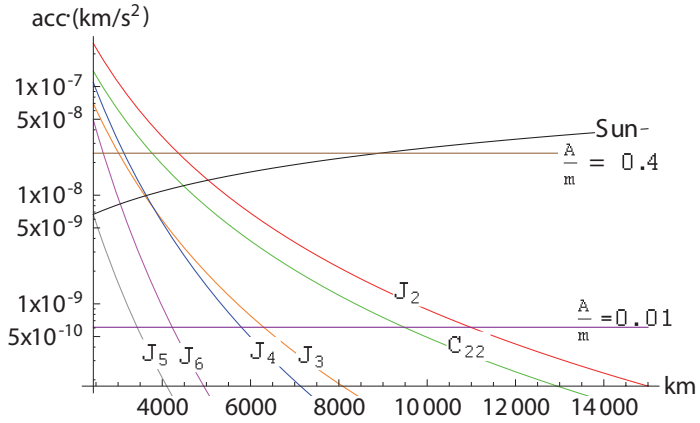

Fig. 3 Orders of magnitude (perturbations) as functions of the distance from Mercury's center (log scale)

in eccentricity may be due either to the effect of higher zonal harmonics on a low-altitude satellite, or to the third-body effect on a high-altitude satellite.

In particular, the oblateness of the planet, J_2, causes orbital plane precession and the rotation of the argument of pericenter. Odd J_3 harmonic mainly affects the eccentricity and the argument of pericenter, while the semimajor axis and the orbital plane remain constant. Even J_4 harmonic produces variations of the same order of magnitude than J_3 harmonic (see Fig. 3). And, as it can be seen in the figure, the magnitude of these perturbations decreases as the degree of the zonal harmonic increases. Regarding the equatorial ellipticity $\overline{C}_{22}$, the variability of the right ascension of the ascending node (dependent on the angular velocity of the planet) implies that the perturbation has a periodical character, which may give rise to long-period perturbation due to commensurability of the orbital period of the satellite and the rotational period of the central planet [31].

On the other hand, third-body perturbation makes the orbit to flatten in the direction of the perturbing body. It produces secular effects on the argument of pericenter and the right ascension of the ascending node. It mainly affects the dynamics of high altitude satellites.

Finally, the effect of solar radiation pressure is non-negligible, especially for those satellites that have a large surface exposed to the Sun's rays. If it is not properly taken into account, it might cause the orbiter to either crash into the planet or get ejected from orbit. In the case of Mercury, it has been proved that the radiation pressure from the Sun generates a perturbing acceleration of two orders of magnitude less than the $\overline{C}_{22}$ effect (Milani and Gronchi [25]). Nevertheless, this statement depends on the satellite's altitude and its surface.

To sum up, zonal gravity terms, third body perturbation and radiation pressure produce periodic variations in all orbital elements while only angular orbital elements Ω and ω suffer from secular effects. On the other hand, tesseral gravity term only produces periodic variations. Nonetheless, coupling effects may imply that, for example, oscillations in the eccentricity cause lowering the pericenter altitude.

Apart from these perturbations, the reader is referred to Milani and Gronchi [25] that shows a complete list of all perturbations acting on Mercury. These authors state that the planetary albedo of Mercury, thermal emission from the planet and from the spacecraft itself, tides and general relativity corrections are of lower orders of magnitude than the perturbations considered in this work. Consequently, we stress out that our proposed dynamical scenario, although simplified, is accurate enough for the purpose of computing frozen orbits around Mercury.

3 Averaging procedure

We calculate the motion of the spacecraft numerically integrating the Lagrange planetary equations that govern the variation of the osculating orbital elements [15]. We are interested in the computation of frozen orbits, which are those whose orbital eccentricity and argument of pericenter remain constant on average. The equations of motion of this dynamical system involve two types of periodic terms: one contains the period of the probe and the other contains the orbital period of Mercury around the Sun. In this context, the motion of the satellite is studied under the double-averaged analytical model with the aim of reducing the degrees of freedom of the system and eliminating the short-period terms of the disturbing function.

Hence, we apply a two-fold process that firstly averages over the period of the satellite and secondly averages with respect to the period of the third body,

$$\langle F \rangle = \frac{1}{2\pi} \int_0^{2\pi} F \; dM, \tag{13}$$

where M stands for the mean anomaly. The development of the equations has been carried out in closed form to avoid expansions in eccentricity and inclination. Details of the application of this technique can be found in Tresaco et al. [28] and Carvalho et al. [4]. The resulting expressions are derived in Appendix 6.1. We depict here the result of the averaged potential of the tesseral term $\overline{C}_{22}$ given in Eq. (6).

$$\langle R_{C_{22}} \rangle = -\frac{3}{2} \overline{C}_{22} R_M^2 \, \frac{n^2}{(1-e^2)^{3/2}} ({c_i}^2 - 1) \cos\left(2(\Omega - \gamma_M \, t)\right). \tag{14}$$

Second average is applied with respect to the third-body orbital period. Note that the orbital elements of the spacecraft are constant during this averaging process, thus

$$\langle\langle R_{C_{22}} \rangle\rangle = \langle R_{C_{22}} \rangle.$$

Hence, the secular disturbing potential of the orbital motion is given by the addition of the averaged perturbation terms, named R (explicit equations are listed in Appendix 6.1),

$$R = \langle\langle R_{J_2} \rangle\rangle + \langle\langle R_{J_3} \rangle\rangle + \langle\langle R_{J_4} \rangle\rangle + \langle\langle R_{J_5} \rangle\rangle + \langle\langle R_{J_6} \rangle\rangle + \langle\langle R_{C_{22}} \rangle\rangle + (1-\beta)\langle\langle R_{3b} \rangle\rangle. \tag{15}$$

Note that the term $\langle\langle R_{SRP} \rangle\rangle$ is not listed in Eq.15 because it has been combined with the Sun gravitational perturbation after the double-averaging process (see their expressions in Appendix 6.1).

4 Frozen orbits computation

For observation and reconnaissance missions it is important to maximize the quality of the data collected from on-board instruments. Therefore, the orbit has to be carefully selected in order to minimize the influence of orbital perturbations. As we have explained in Section 2.4, most satellites experience noticeable variations in orbital elements under the influence of orbital perturbations. Some studies about BepiColombo extended mission state that the pericenter of MPO orbiter is expected to drift from the initial 15°N up to 70°S in three years, and the pericenter altitude is expected to decrease from 480 to 250 km [13]. Consequently, altitude control for an extended mission would require a continuous orbital maintenance. Nevertheless, the number of corrective manoeuvres can be dramatically reduced by a careful selection of the orbital parameters. By designing an orbit for which the mean eccentricity and mean argument of pericenter remain static, the satellite altitude will be constant and it will ensure a longer lifetime. This is called a frozen orbit. Earth's frozen orbits have been extensively studied in the past. In the case of the Moon, asteroids or other planets, interest in frozen orbits has developed recently.

The classical approach of computation of frozen orbits is based on the manipulation of the Lagrange planetary equations that describe temporal variation of the orbital elements. To design a frozen orbit, the secular variations of the eccentricity and argument of pericenter caused by orbital perturbations have to be zero. Hence, the disturbing function is introduced in the Lagrange planetary equations after eliminating short-period terms. Frozen orbits are identified as the equilibrium points of these equations. Generally, this procedure is only based on the zonal terms of the spherical harmonics. If the value for frozen eccentricity is assumed to be small, a closed equation for the eccentricity is obtained for given values of the semimajor axis and inclination (Vallado [29]):

$$e = \pm \frac{\displaystyle\sum_{k=1}^{\infty} \left(k J_{2k+1} \left(\frac{R_M}{a} \right)^{2k+1} \sum_{l=1}^{k} D_l^{2k+1} s_i^{2k+1-2l} \right)}{\displaystyle\sum_{k=1}^{\infty} J_{2k} \left(\frac{R_M}{a} \right)^{2k} (X + Y + Z)}, \tag{16}$$

where

$$X = 2c_i^2 \sum_{l=0}^{k-1} (k-l) A_l^{2k} s_i^{2k-2l-2}, \qquad A_n^m = \frac{(2n-2m)!(-1)^m}{m!(n-m)! \left(\frac{n}{2}-m\right)! \left(\frac{n}{2}-m\right)! \, 2^{2n-2m}},$$

$$Y = -k(2k-1) \sum_{l=0}^{k} A_l^{2k} s_i^{2k-2l}, \qquad D_n^m = \frac{(2n-2m)!(-1)^m}{m!(n-m)! \left(\frac{n-1}{2}-m\right)! \left(\frac{n+1}{2}-m\right)! \, 2^{2n-2m}},$$

$$Z = -(k-1)(2k-1) \sum_{l=0}^{k-1} E_l^{2k} e s_i^{2k-2l}, \qquad E_n^m = \frac{(2n-2m)!(-1)^m}{m!(n-m)! \left(\frac{n-2}{2}-m\right)! \left(\frac{n+2}{2}-m\right)! \, 2^{2n-2m}}.$$

This expression is valid in zonal potential models to an arbitrary degree. The ± sign depends on the signs of the coefficients and should be chosen such that the final value be positive. Fig. 4 shows the variation in frozen eccentricity as a function of the zonal terms in case of a satellite with an inclination of 90.4° and

an altitude of 500 km. It represents the cumulative effect of the zonal coefficients (first blue square means that only J_2 and J_3 are used in Eq. (16), second square means $J_2 + \cdots + J_5$, and so on). Thus, we observe that we need to include at least the first seven terms to improve the value of the first predicted eccentricity (only with J_2 and J_3) up to 20%.

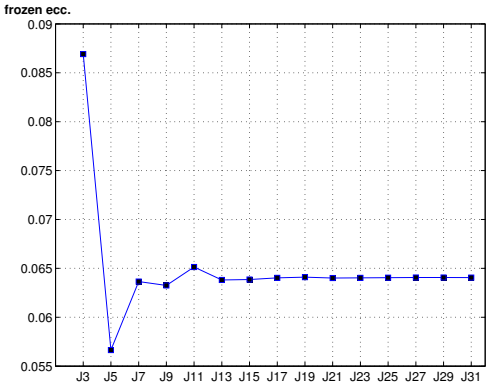

Fig. 4 Frozen eccentricity value depending on the degree of zonal harmonics considered. Gravity field model HgMUCLA40x40, Verma 2016 [30].

This procedure of using the Lagrange planetary equations for an averaged perturbing function can be repeated for more realistic perturbation models and, although, the resulting expressions will nowhere near elegant, they can be solved numerically. For a complete theory, we must average the Hamiltonian model proposed to eliminate short-period terms. Afterwards, the secular variations of the eccentricity and argument of pericenter caused by orbital perturbations listed in Section 2 have to be zero. Thence, the resulting expressions for a given disturbing function R are

$$\begin{aligned} \frac{d\omega}{dt} &= \frac{-\sqrt{1-e^2}}{n\,a^2 e}\,\frac{\partial R}{\partial e} + \frac{\cot i}{n\,a^2\sqrt{1-e^2}}\,\frac{\partial R}{\partial i}, \\ \frac{de}{dt} &= \frac{\sqrt{1-e^2}}{n\,a^2 e}\,\frac{\partial R}{\partial \omega} - \frac{1-e^2}{n\,a^2\,e}\,\frac{\partial R}{\partial M}. \end{aligned} \tag{17}$$

The expression of the double-averaged potential R given in Eq. (15) that must be replaced on the previous system Eq. (17) is depicted in the Appendix 6.1. Remark that this double-averaged potential does not include the C_{22} term. Thus, frozen orbits are found as the equilibria of this system of equations:

$$\frac{d\omega}{dt} = 0, \quad \frac{de}{dt} = 0. \tag{18}$$

So, the final stage is undertaken by solving this system of equations. Using this approach, it is possible to have a three-dimensional surface parametrized by (a, e, i) whose points are initial conditions of frozen orbits. Once we have computed these orbits, the C_{22} term will be included in the numeric integrations in order to visualize its effect on the frozen orbits (see Sec. 4.2). Note that all the calculations

along the paper were performed in Maple software and C language. In particular, we used the numerical integrator dopri853 (Runge-Kutta order 8(5,3) with dense output of order 7).

Frozen orbits have been extensively studied in the past. In this context, we can find in literature various criteria in order to characterize and illustrate frozen orbits. In particular, we will use the following ones:

- Frozen location
  - 3-D surfaces (a, e, i): points on this surface correspond to equilibria of the reduced system.
  - Curves for constant-a: orbital altitude is fixed in order to go into more detail.
- Frozen character
  - Representation of the quantities $(e\cos\omega, e\sin\omega)$. These figures exhibit closed-circle trajectories centred on the frozen orbit values.
  - Contour plots to visualize a discrete set of frozen solutions and their stability.
  - Long-term propagations: numeric simulations in the original system of the averaged frozen conditions.

4.1 **Analysis without** C_{22}

As it is stated above, the equilibria of the equations of motion of the reduced Hamiltonian given in Eq. (18) correspond to frozen orbit conditions. If we only consider the non-spherical zonal perturbation of Mercury, the second equation ($de/dt = 0$) clearly nullifies when $\omega = \pi/2, 3\pi/2$ (see Appendix 6.2). This is due to the fact that even zonal terms J_n imply trigonometric terms $\sin((n-2)\,\omega)$, while if n is odd it appears $\cos((n-2)\,\omega)$. Therefore, $\omega = \pi/2$, and $\omega = 3\pi/2$ cancel out a combination of disturbing zonal terms. When we consider third-body and solar pressure perturbations the cancellation of de/dt also requires that $\Omega - \Omega_\odot = 2k\pi$, $k \in \mathbb{Z}$. Without loss of generality, we can assume the inertial frame with the x-axis in coincidence with the apsidal line of the third-body motion at the initial time. This means $\Omega_\odot = 0$ and $f_\odot = 0$. Hence, we set $\omega = \pi/2, 3\pi/2$ to nullify the eccentricity variation. Then, these values of ω are plugged in equation $d\omega/dt = 0$ that depends on three variables: the orbital eccentricity e, inclination i, and semi-major axis a. This equation represents a surface; points on this surface correspond to equilibria of the system (Eq. (18)), that is, to initial conditions (a, e, i) of frozen orbits.

The following figures depict the location and behaviour of frozen orbits. The results are first analysed in terms of the different disturbing functions (see Fig. 5 and Fig. 6), where we depict the initial conditions (e, i) of frozen orbits for a given altitude. Note that the horizontal line that appears in the following graphs represents the limit for impact orbits. The higher the eccentricity is, the shorter is the distance at the pericenter. Thus, the impact value is the eccentricity value that makes the distance at the pericenter shorter than Mercury's radius. Consequently, the orbital eccentricity must be lower than the impact value to avoid possible collisions with the planet surface.

Figures 5 (a-d) represent the effect of the zonal harmonics. Plots (a) and (b) are important because they highlight the change in the behaviour of low eccentric orbits. There is a decrease in the value of frozen eccentricity when we include the harmonic J_4. Then, J_5 slightly produces any modification due to its small value compared to the other terms (Fig. 5 (c)). Nevertheless, the inclusion of J_6 is again important, see Fig. 5 (d). At $\omega = \pi/2$, the frozen inclinations were only concentrated in the vicinity of $i = 0^\circ$ or the critical inclination of the satellite ($\cos^2 i = 1/5$) i.e. $i = 67.0492^\circ$. However, J_6 magnitude allows to find near polar eccentric frozen orbits.

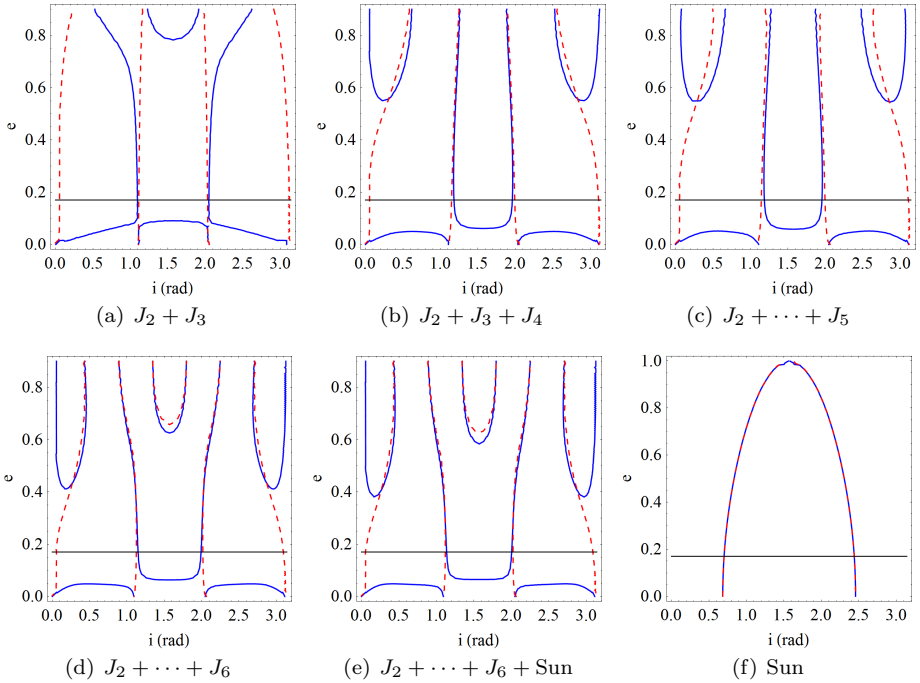

(a) $J_2 + J_3$ (b) $J_2 + J_3 + J_4$ (c) $J_2 + \cdots + J_5$

(d) $J_2 + \cdots + J_6$ (e) $J_2 + \cdots + J_6 + \text{Sun}$ (f) Sun

Fig. 5 Section (i, e) of frozen orbits with altitude of 500 km. Blue line: $\omega = 3\pi/2$, red dashed line: $\omega = \pi/2$.

These results have been validated using the work performed by Mazarico et al. [22], in particular, they presented the computation of frozen orbits when only the zonal gravity coefficients of their estimated gravity field, termed HgM005 (2014), were considered.

Summarizing, as long as we consider more terms in the gravity field of Mercury, the frozen orbits at $\omega = \pi/2$ are closer to the critical inclination value of the satellite. Moreover, the eccentricity value on the higher branch at the polar region decreases, while the eccentricity on the lower branch increases. In conclusion, although the secular effects of the gravitational zonal terms are reduced with degree and altitude (see Fig. 3), the figures obtained confirm that J_2 and J_3 are not sufficient to predict the location of frozen orbits about Mercury.

Regarding the effect of the Sun's perturbation, we observe that the inclusion of third-body in the dynamical model (Fig. 5 (e)) does not imply dramatic changes. This is due to the fact that these figures are computed for a low-altitude orbit. The real effect of the Sun's gravity perturbation can be seen in Fig. 8, where different altitudes are represented.

Now, we move to the complete dynamical model that includes the zonal gravity field up to sixth degree, the gravitational attraction of the Sun and SRP. In Fig. 6 we have computed the frozen eccentricity for a fixed altitude of 2000 km and two values of the area-to-mass ratio, in order to visualize the effect of solar radiation pressure perturbation. Thus, we see that, when A/m increases, the maximum value of frozen eccentricity is greater when approaching polar orbits.

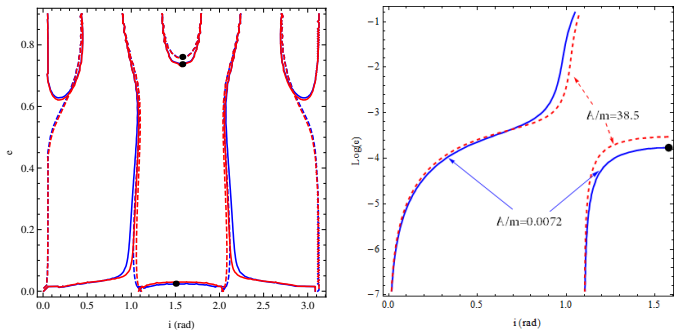

Fig. 6 Frozen orbits for an altitude of 2000 km and $A/m = 7.2 \cdot 10^{-3}$ m^2/kg (MMO) in blue colour, and $A/m = 38.5$ m^2/kg (Sunjammer) in red. Dashed line: $\omega = \pi/2$, solid line: $\omega = 3\pi/2$. Right plot: zoom of the non-impact region for $i \in (0, \pi/2)$ and eccentricity in logarithmic scale. Dots represent initial conditions extracted for stability analysis.

Figures 7 and 8 are obtained for SRP coefficient $\beta = 0.01$ (an intermediate value between the A/m coefficients represented in Fig. 6). Fig. 7 represents the surface that correspond to equilibria of this dynamical system, that is, to initial conditions (a, e, i) of frozen orbits.

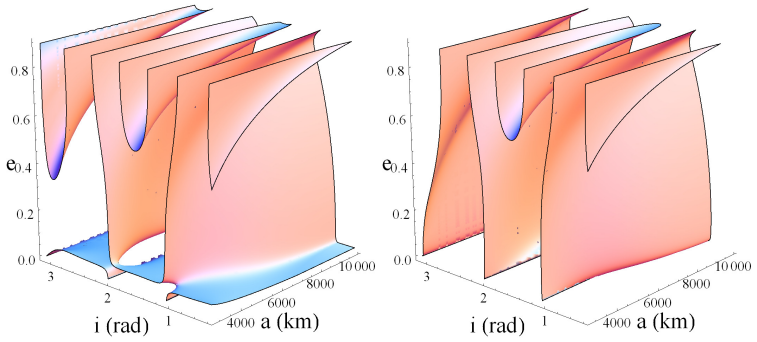

Fig. 7 Surface of frozen orbits for $\omega = 3\pi/2$ and $\omega = \pi/2$ respectively.

In order to go into more detail, the orbital altitude is fixed. Figure 8 depicts the location of frozen eccentricity for increasing altitudes (500, 3000 and 6000 km). The eccentricity is in logaritmic scale, and its range is limited to non-impact orbits. The inclination is varied up to 90° thanks to the symmetry of the sections of frozen orbits.

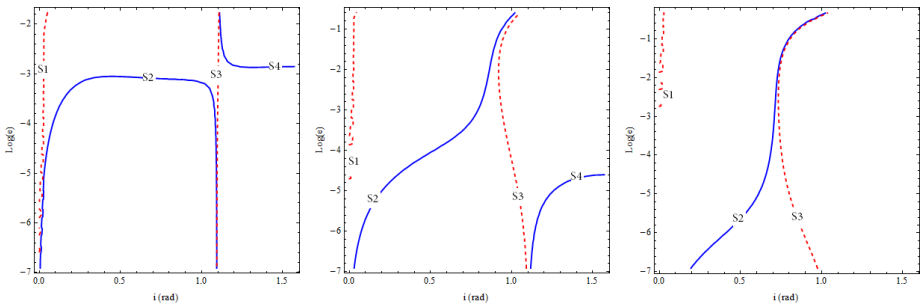

(a) Altitude 500 km. (b) Altitude 3000 km. (c) Altitude 6000 km.

Fig. 8 The logarithm of frozen eccentricities vs. inclinations for an altitude range of 500, 3000 and 6000 km. Blue line: $\omega = 3\pi/2$, red dashed line: $\omega = \pi/2$.

In this figure, we can observe that, for high-altitude orbits, the Sun exerts a large perturbation and dominates the dynamic. Fig. 8(a) shows that frozen orbits at all inclinations can be derived. Four families of frozen orbits are discovered. S_1 begins with a quasi-circular equatorial orbit with argument of pericenter equal to $\pi/2$, but soon, the eccentricity grows to the impact region. Family S_2 has small eccentricity and the argument of pericenter equal to $3\pi/2$. It begins with circular planar orbits, then the inclination increases until its termination with orbits of critical inclination. Then, family S_3 appears. This family, with the argument of pericenter equal to $\pi/2$, is composed of orbits on a small range of inclination close to the critical value, and eccentricities that change rapidly from an ellipse to a circle. Finally, polar frozen orbits with $\omega = 3\pi/2$ belong to family S_4. As it can be seen, when the altitude increases, the behaviour of near circular orbits changes. In addition to the critical inclination of the satellite, the critical inclination of the third-body problem ($\cos^2 i = 3/5$) i.e $i = 55.1736°$, also plays a role. As long as the altitude takes higher values, the region of non-impact orbits is dramatically reduced, families S_2 and S_3 merge at the value of the critical inclination of third-body, while family S_4 disappears. Thus, the existence of frozen orbits is limited to the critical inclination of the third-body interval: $i \in (0.684719, 2.45687)$ rad. This phenomenon is clearly observed in Fig. 5 (f), where only the Sun perturbation is considered. In this case, the curves $\omega = \pi/2$ and $\omega = 3\pi/2$ completely overlap. Note also that non-impact frozen orbits at polar inclination exist for all altitudes, and their eccentricity values decrease with the altitude.

Lastly, frozen orbits exist for many of the inclinations and semimajor axis values. If we focus on near-polar orbits, which are interesting because they could provide global coverage, we observe the following behaviour. Limiting to the non-impact regions, outside of a narrow range near the critical inclination values of the satellite and the third-body, the majority of useful frozen orbits obtained have

argument of pericenter of 270°. That is, the pericenter of the orbit is near the south pole. This is due to the fact that J_3 is dominant among the odd degree zonals and it has the same sign than J_2 (as in the case of the Moon).

With regard to stability, the character of the frozen orbits may be ascertained either from the evaluation of the Jacobian matrix of the averaged Hamiltonian or from the graphic representation of the reduced flow, where elliptic fixed points correspond to stable equilibria and hyperbolic fixed points to unstable equilibria. For example, Fig. 9 shows the stability character of some polar frozen orbits encountered.

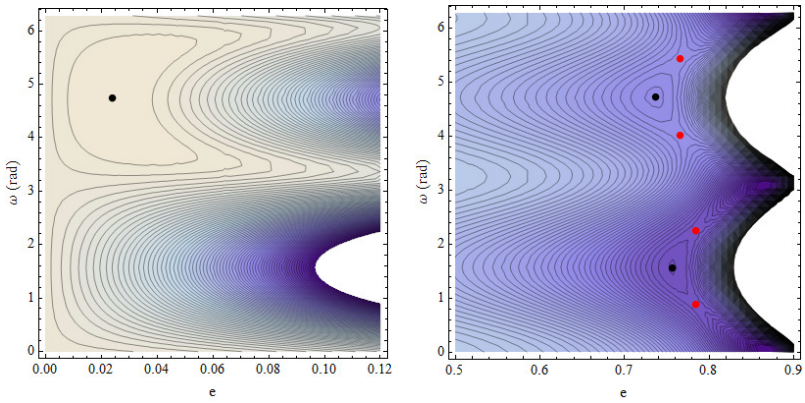

Fig. 9 Phase portrait of polar frozen orbits for an altitude of 2000 km and $A/m = 7.2 \cdot 10^{-3}$ m^2/kg. Left plot depicts low eccentricity map and right plot is for high values of the eccentricity. Dots represent equilibrium points (black color means stable points and red color unstable).

Thus, following our initial conditions, extracted from Fig. 6, the three black dots correspond to frozen polar orbits. Figure 9 allows us to identify them as two stable equilibrium with $\omega = 270°$ ($e = 0.023$ and $e = 0.736$) and one stable equilibrium with $\omega = 90°$ ($e = 0.758$). Besides, we also get four unstable equilibria in the right plot of Fig. 9 (red dots). Two of them with eccentricity $e = 0.78$ (for $\omega = 49°$ and $\omega = 129°$), and another two with eccentricity $e = 0.76$ (for $\omega = 229°$ and $\omega = 309°$). All these unstable points correspond to orbits in the impact region due to their large eccentricity value. It is important to point out that these unstable frozen orbits are not represented in Fig. 6 because it only depicts the "easiest cases" of $\omega = \pi/2, 3\pi/2$. Examples of the analytical treatment of the case $\cos\omega \neq 0$ that nullifies de/dt for simplified dynamical models can be found in Abad [1] and Delsate et al. [8].

Another example of phase portrait representation is shown in Fig. 11, where we have fixed two different values of the ratio between the inclination and eccentricity: $\eta = \sqrt{1-e^2}\cos i$, equal to $\eta = 0.95$ and $\eta = 0.41$. For each value of η we can obtain a discrete number of frozen orbits. In these particular cases we get two stable equilibrium (elliptic points) that can be identified as black dots in Fig. 10, and an unstable orbit (hyperbolic point) marked in red. These three points correspond

to frozen orbits with altitude 400 km and the following orbital elements (e, i, ω): $(0.275, 8.8°, 90°)$, $(0.05, 17.9°, 270°)$ and $(0.074, 65.7°, 270°)$.

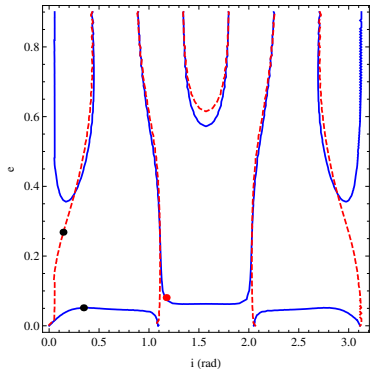

Fig. 10 Section (i, e) of frozen orbits with an altitude of 400km and $A/m = 7.2 \cdot 10^{-3}$ m^2/kg (MMO).

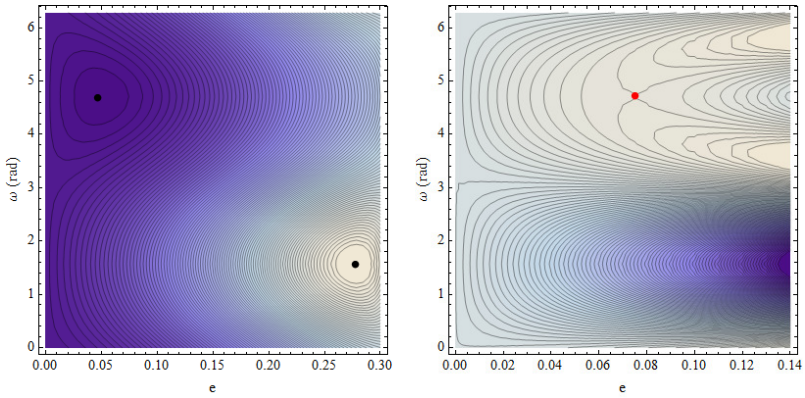

Fig. 11 Phase portrait for an altitude of 400 km and $A/m = 7.2 \cdot 10^{-3}$ m^2/kg. Left plot for $\eta = 0.95$ and right plot for $\eta = 0.41$.

These representations of the eccentricity vector phase space are interesting approaches in order to get the stability of a frozen orbit. They were previously used by Lara et al. (2010) in the analysis of Mercury frozen orbits [17]. Note that the differences in the dynamical model considered in each case make that our phase portraits are quantitatively different from the eccentricity vector phase space shown in their paper. Nonetheless, the use of phase space representations as a stability analysis tool has the drawback that, for each value of the inclination, only a discrete set of frozen orbits exists. Consequently, it does not constitute a systematic procedure to analyse the orbital stability. Next piece of work will be to achieve the stability through the computation of natural families of frozen orbits (Lara et al. [16], Elipe and Lara [9]).

4.2 Effect of C_{22}

Mercury is less flattened than the Earth (see Table 1), which makes the $\overline{C}_{22}$ coefficient to come closer to J_2. In fact, $\overline{C}_{22}$ is the greatest harmonic joined to J_2, so it needs to be considered. If we look at the averaged term corresponding to $\overline{C}_{22}$ in Eq. (14), we observe that it depends on time. Accordingly, we cannot parametrize surfaces (a, e, i) to identify conditions of frozen orbits. Fortunately, we can derive the effect of $\overline{C}_{22}$ applying other techniques.

When we only consider the second order harmonics J_2 and $\overline{C}_{22}$, we get that the critical inclination of the satellite due to the main problem (J_2) may be affected by the $\overline{C}_{22}$ coefficient and by the value of the right ascension of the ascending node Ω. That is, when we replace the corresponding averaged expressions of both perturbing terms in the Lagrange planetary equations (see Eq. (25) and Eq. (26) in Appendix. 6.2) we get the following expression:

$$\frac{d\omega}{dt} = -\frac{3R_M^2\mu^{1/2}}{4a^{7/2}(1-e^2)^2}\left(J_2(5c_i^2-1)+\overline{C}_{22}(6-10c_i^2)\cos(2(\Omega-\gamma_M\,t))\right). \qquad (19)$$

This equation vanishes when

$$c_i^2 = \frac{J_2 - 6\,\overline{C}_{22}\,\cos(2\Omega - 2\,\gamma_M\,t)}{5\,J_2 - 10\,\overline{C}_{22}\,\cos(2\Omega - 2\,\gamma_M\,t)}$$

If we consider the isolated effect of $\overline{C}_{22}$, we find a new critical inclination $c_i^2 = 3/5$. However, when both effects are considered, the new value of the critical inclination is a function of the ratio $J_2/\overline{C}_{22}$ and $\cos(2\Omega - 2\,\gamma_M\,t)$. Fig. 12 represents the value of the inclination and all the valid range for $\cos(2\Omega - 2\,\gamma_M\,t)$ that set $d\omega/dt = 0$. There is a big dependence of the critical inclination with respect to Ω. We observe that the critical inclination value ranges from 58.56° to 90°. And, for some high value of Ω, it will not give rise to a critical inclination. Note that critical inclination orbits are natural frozen orbits (system of Eq. (17) becomes equal to zero). Subsequently, if there is interest in critical inclination orbits, we must take into account the modification of the inclination value due to the tesseral term $\overline{C}_{22}$.

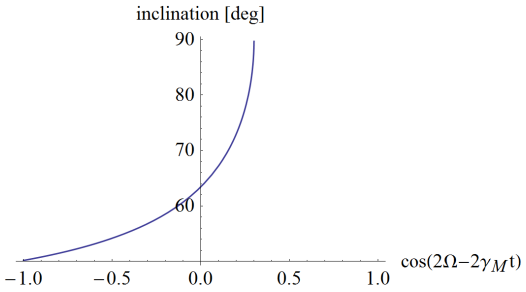

Fig. 12 New value of critical inclination due to the effect of J_2 and $\overline{C}_{22}$.

A deep study about the influence of $\overline{C}_{22}$ in the temporal variation of the eccentricity can be found in Carvalho et al. [5]. In the next section we continue analysing the effect of this tesseral term in the behaviour of frozen orbits.

4.3 Long-term propagations

Orbital stability is important from a practical point of view. A spacecraft in an unstable frozen orbit will impact the planet after a short period of time. Then, the initial conditions of frozen orbits should be carefully considered, as they play an important role on the orbital lifetime. As it has been explained, the main effects from the disturbing functions are secular variations of the eccentricity and argument of pericenter. The following figures present the behaviour for these orbital parameters close to the frozen conditions during 25 years of mission. This approach was also followed by Carvalho et al. [4] and Delsate et al. [8] to show the behaviour of the solutions (orbits) close to the libration equilibrium (frozen orbits). In particular, we derived the results presented in Fig. 10 and 11 of Delsate's paper with their simplified dynamical model in order to test our propagator. Subsequently, following that procedure, Figure 13 presents the libration of the eccentricity and argument of pericenter around an equilibrium point (a low eccentricity polar frozen orbit), whose initial conditions have been extracted from Fig. 6: $a = 4440$ km, $i = \pi/2$, $\Omega = \pi/2$, $\omega = 3\pi/2$. Note that the location of this equilibrium differs from the location presented in the cited Delsate's figures due to the differences in the values of the zonal harmonics. Remember also that these equilibria were obtained for the time-independent averaged system i.e. without the $\overline{C}_{22}$ perturbation. We observe in Fig. 13 that the equilibrium point corresponds to the frozen eccentricity value $e = 0.023$. In the vicinity of this equilibrium the eccentricity vector describes a rotation, this known behaviour is the basis of most passive eccentricity control strategies.

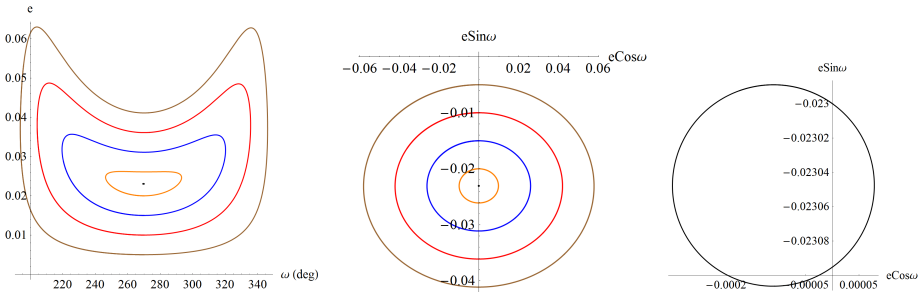

(a) (e, ω) diagram (b) eccentricity vector (c) equilibrium

Fig. 13 (e, ω) diagram (a) and eccentricity vector representation (b,c) for different initial conditions. (c)-plot: zoom of the eccentricity vector for the equilibrium point $e = 0.023$.

If we add the perturbation due to the tesseral $\overline{C}_{22}$ term, we observe that the eccentricity of the frozen orbit decreases, from 0.023 to 0.00985. Fig. 14 shows the behaviour for different initial conditions close to the frozen eccentricity value.

In addition to this, Fig. 15 presents the long-term evolution over 25 years of the eccentricity, argument of pericenter, and altitude of pericenter when $\overline{C}_{22}$ tesseral is included. Along that period of time, the eccentricity averages to 0.00975, which is very close to the frozen value 0.00985. We observe that the orbital elements remain frozen on average. The pericenter altitude is very stable, varying only by

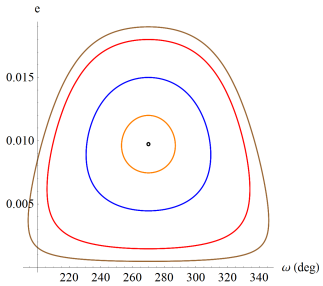

Fig. 14 (e, ω) diagram when $\overline{C}_{22}$ perturbation is included.

one km over the 25 year orbit integration. However, it is important to remark that the long-term propagation is computed from the averaged orbital elements. Since we are not recovering the non-averaged model. Subsequently, the periodic oscillations observed in Fig. 15 are due to the elimination of periodic terms in the double-averaging process.

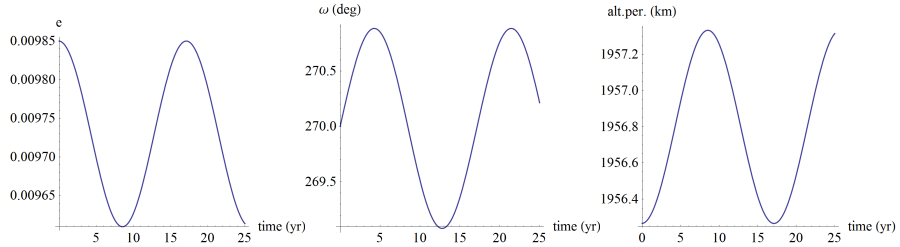

Fig. 15 Frozen orbit long-term propagation for the complete dynamical model. Initial conditions $a = 4440$ km, $e = 0.00985$, $i = \pi/2$, $\Omega = \pi/2$, $\omega = 3\pi/2$.

We perform a similar test to unstable frozen orbits. We extract the orbital parameters for the hyperbolic point of Fig. 11. The long-term propagation of its initial conditions: $a = 2840$ km, $e = 0.0737609$, $i = 65.72°$, $\Omega = \pi/2$, $\omega = 3\pi/2$, is shown in Fig. 16.

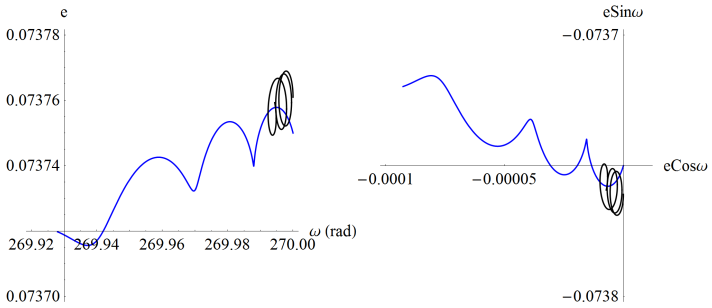

Fig. 16 (e, ω) diagrams and eccentricity vector representation for initial conditions close to an unstable frozen orbit (black).

It depicts the frozen orbit (black curve) and a very close orbit with an eccentricity equal to 0.07375 (blue curve). We observe that the unstable character unfrozens the orbit after a few years.
Finally, Fig. 17 shows the behaviour of the eccentricity of a frozen orbit when different terms of the perturbation function are considered. Frozen eccentricity value is computed from the simplest case, considering only J_2 and J_3 harmonics (Eq. 16). The initial conditions are $a = 4440$ km, $e = 0.058$, $i = \pi/2$, $\Omega = \pi/2$, $\omega = 3\pi/2$. Then, we have integrated these initial conditions for different dynamical models in order to show that it is important to provide a good approximation to the real dynamics. **Note that we have considered a large SRP value of A/m=10 m^2/kg in order to highlight its effect.**

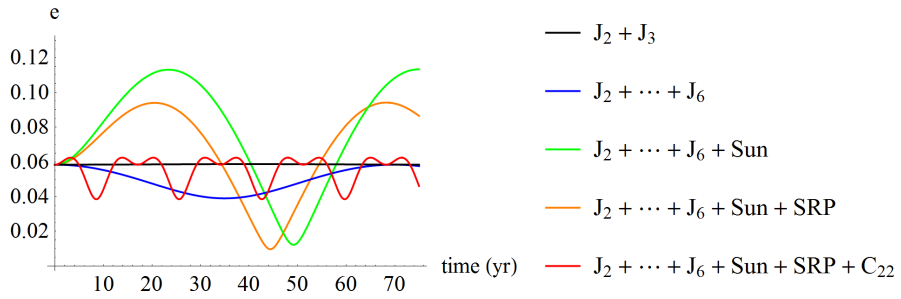

Fig. 17 Long-term evolution of the frozen eccentricity for different disturbing terms.

We can also observe in this figure a known effect (see details in Lidov [18]). Although third-body effect makes the eccentricity to increase, perturbations due to the non-sphericity of the central planet may counterbalance the planetary perturbations to some extent. That means, higher gravitational inhomogeneities may extend the lifetime of a satellite as they counteract the third-body effect. Besides, as we have seen previously, coupling effects due to $\overline{C}_{22}$ perturbation may imply that the periodic oscillations produced in the eccentricity cause lowering the pericenter altitude. To sum up, in order to provide useful information for mission-planning purposes, it is important to incorporate the most important disturbing effects in the Hamiltonian dynamical model.

5 Conclusions

The location of frozen orbits is essential for understanding the dynamics of non-integrable system, and for efficient design of Mercury's orbiter missions, since minimal orbital control is required in the vicinity of that kind of orbits. In order to determine the initial conditions of the frozen orbits, we apply averaging techniques. Frozen orbits are found as equilibria of the equations of motion after the elimination of short-period terms. These terms are due to disturbing forces acting on the orbiting probe. The case of the motion around Mercury is mainly governed by the gravitational attraction of the main body and the Sun, whose orbit exhibits a non-negligible eccentricity. In this approach, we use the recent MESSENGER

gravity determination [30] to update previous works where we considered simplified models. Tesseral term $\overline{C}_{22}$ reveals to be the greatest harmonic joined with J_2, so it is included in the proposed dynamical model. These improved values of the harmonic coefficients imply modifications in the initial orbit design.

Along this paper, we have provided different criteria to analyze frozen orbits around Mercury, and to examine their basic nature. Using the techniques described above, we have obtained a set of surfaces that characterize frozen orbits depending on three variables: the orbital semimajor axis, eccentricity and inclination. Some important facts emerge from Figures 7, 5 and 8. (i) For low and moderate-high altitudes, there are frozen orbits over all the range of inclinations. We have identified four different families of frozen orbits, labelled S_1, S_2, S_3 and S_4. (ii) The critical point in the family S_3 occurs close to the critical inclination of the satellite. However, as long as the altitude increases, this inclination value migrates to the left i.e. decreases. The reason for this decrease is the reduction in strength of the perturbation caused by the gravitational harmonics as they are inversely proportional to powers of the altitude. This could be an interesting location for missions requiring frozen circular orbits. (iii) For very high altitudes, the Sun attraction dominates and consequently, there are only frozen orbits in the interval limited by the critical inclination of the third-body. (iv) The majority of useful frozen orbits obtained have the pericenter near the south pole ($\omega = 270°$). This is because J_3 is dominant among the odd degree zonals and it has the same sign than J_2.

On the other hand, concerning the effect of solar radiation pressure, we observe that it produces a characteristic acceleration 10 times greater than for the same satellite orbiting the Earth. We have seen that, for probes with large area-to-mass coefficient, this perturbation mainly affects frozen polar orbits increasing the value of their eccentricity. This is due to the fact that the value of frozen eccentricity drops because of the third body attraction exerted by the Sun, and we have assumed that solar pressure is a constant force acting in anti-solar direction.

Furthermore, the orbital stability has been portrayed in phase portrait diagrams, these figures together with long-term propagations give us the behaviour of frozen orbits. Thus, we have observed that higher gravitational terms may counteract the third-body perturbation and so, extend the orbit lifetime. Moreover, the effect due to equatorial ellipticity of Mercury contributes strongly to maintain the frozen orbits for low-altitude orbits.

Finally, this paper provides initial conditions of frozen orbits that can be used for numerical correction methods in more complex models. Because the averaging procedure applied to this problem is analytic, this approach is not restricted to the case of the motion about Mercury, and may be applied to other dynamical systems.

Acknowledgments

This research has been funded by the Spanish Ministry of Economy and Competitiveness (code #ESP2013-44217-R) and the support of CNPq, National Council for Scientific and Technological Development - Brazil (N°306953/2014-5, 420674/2016-0). J. P. S. Carvalho thanks professor Tadashi Yokoyama by his support in clarifying some points of the paper.

6 Appendix

6.1 Double-averaged disturbing functions

This appendix shows the expressions of the double-averaged Hamiltonian. This is a two-fold procedure which firstly averages over the orbital period of the spacecraft and secondly averages with respect to the third body period. Details can be found in Tresaco et al. [28].

$$
\begin{aligned}
\langle\langle R_{J_2}\rangle\rangle &= -\frac{1}{4}\,R_M^2\,J_2\frac{n^2}{(1-e^2)^{3/2}}(-2+3s_i^2),\\
\langle\langle R_{J_3}\rangle\rangle &= -\frac{3}{8}\,R_M^3\,J_3\frac{n^2\,s_i\,e}{a(1-e^2)^{5/2}}\,(-4+5s_i^2)\,\sin\omega,\\
\langle\langle R_{J_4}\rangle\rangle &= \frac{3}{128}\,R_M^4\,J_4\frac{n^2}{a^2(1-e^2)^{7/2}}\left(10\,e^2s_i^2(7s_i^2-6)\cos(2\omega)-(3e^2+2)(35s_i^4-40s_i^2+8)\right),\\
\langle\langle R_{J_5}\rangle\rangle &= \frac{5}{256}\,R_M^5\,J_5\frac{n^2\,s_i\,e}{a^3(1-e^2)^{9/2}}\left(14e^2s_i^2(9s_i^2-8)\cos(2\omega)+e^2(-315s_i^4+448s_i^2-144)\right.\\
&\quad\left.-24(21s_i^4-28s_i^2+8)\right)\sin\omega,\\
\langle\langle R_{J_6}\rangle\rangle &= -\frac{5}{4096}R_M^6\,J_6\frac{n^2}{a^4(1-e^2)^{11/2}}\left(-2(15e^4+40e^2+8)(231s_i^6-378s_i^4+168s_i^2-16)\right.\\
&\quad\left.-63e^4(11s_i^2-10)s_i^4\cos(4\omega)+210e^2(e^2+2)(33s_i^4-48s_i^2+16)s_i^2\cos(2\omega)\right),\\
\langle\langle R_{C_{22}}\rangle\rangle &= \frac{3}{2}\,R_M^2\,\overline{C}_{22}\frac{n^2}{(1-e^2)^{3/2}}\,s_i^2\,\cos(2(\Omega-\gamma_M t)).
\end{aligned}
\tag{20}
$$

For the third-body and SRP we have the disturbing terms (Liu et al. [19]) written in terms of the coefficients α and γ given by:

$$
\begin{aligned}
\alpha &= \cos\omega\cos(\Omega-\Omega_\odot)\cos f_\odot+\sin i\sin i_\odot\sin\omega\sin f_\odot+\cos\omega\cos i_\odot\sin(\Omega-\Omega_\odot)\sin f_\odot\\
&\quad-\sin\omega\cos i\sin(\Omega-\Omega_\odot)\cos f_\odot+\sin\omega\cos i\cos i_\odot\cos(\Omega-\Omega_\odot)\sin f_\odot.\\
\gamma &= -\sin\omega\cos(\Omega-\Omega_\odot)\cos f_\odot+\sin i\sin i_\odot\cos\omega\sin f_\odot-\sin\omega\cos i_\odot\sin(\Omega-\Omega_\odot)\sin f_\odot\\
&\quad-\cos\omega\cos i\sin(\Omega-\Omega_\odot)\cos f_\odot+\cos\omega\cos i\cos i_\odot\cos(\Omega-\Omega_\odot)\sin f_\odot.
\end{aligned}
\tag{21}
$$

Rewritting α and γ as $\alpha=\alpha_1\cos f_\odot+\alpha_2\sin f_\odot$ and $\gamma=\gamma_1\cos f_\odot+\gamma_2\sin f_\odot$,

$$
\begin{aligned}
\alpha_1 &= \cos\omega\cos(\Omega-\Omega_\odot)-\sin\omega\cos i\sin(\Omega-\Omega_\odot),\\
\alpha_2 &= \sin i\sin i_\odot\sin\omega+\cos\omega\cos i_\odot\sin(\Omega-\Omega_\odot)+\sin\omega\cos i\cos i_\odot\cos(\Omega-\Omega_\odot),\\
\gamma_1 &= -\sin\omega\cos(\Omega-\Omega_\odot)-\cos\omega\cos i\sin(\Omega-\Omega_\odot),\\
\gamma_2 &= \sin i\sin i_\odot\cos\omega-\sin\omega\cos i_\odot\sin(\Omega-\Omega_\odot)+\cos\omega\cos i\cos i_\odot\cos(\Omega-\Omega_\odot).
\end{aligned}
\tag{22}
$$

we get the following equations after averaging:

$$
\langle\langle R_{3b}\rangle\rangle = \frac{3a^2n_\odot^2}{4\left(1-e_\odot^2\right)^{3/2}}\Big(\frac{\alpha_1^2+\alpha_2^2}{2}(1+4e^2)+\frac{\gamma_1^2+\gamma_2^2}{2}(1-e^2)-\big(\frac{2}{3}+e^2\big)\Big).
\tag{23}
$$

$$
\langle\langle R_{SRP}\rangle\rangle = -\beta\frac{3a^2n_\odot^2}{4\left(1-e_\odot^2\right)^{3/2}}\Big(\frac{\alpha_1^2+\alpha_2^2}{2}(1+4e^2)+\frac{\gamma_1^2+\gamma_2^2}{2}(1-e^2)-\big(\frac{2}{3}+e^2\big)\Big).
\tag{24}
$$

6.2 Lagrange equations of averaged disturbing functions

The disturbing double-averaged function, named R and given in Eq. 15, is the sum of each term shown in Appendix 6.1. Frozen orbits are the zeros of the Lagrange planetary equations that give the secular variation of e and ω, (see Eq. (17)). Now, we present here the expression of these equations. For the sake of clarity, it is shown in three parts, for the zonal contribution, for the tesseral term $\overline{C}_{22}$ and for the Sun plus SRP perturbations.

– Zonal disturbing function: $\langle\langle R_{J_2}\rangle\rangle + \langle\langle R_{J_3}\rangle\rangle + \langle\langle R_{J_4}\rangle\rangle + \langle\langle R_{J_5}\rangle\rangle + \langle\langle R_{J_6}\rangle\rangle$.

$$
\begin{aligned}
\frac{d\omega}{dt} = & -J_2\,\frac{3R_M^2 n(5\cos 2i+3)}{8a^2(e^2-1)^2} + J_3\,\frac{3R_M^3 n\csc i\sin\omega\left(5(7e^2+1)\cos 4i-3e^2-4\cos 2i-1\right)}{64a^3e(1-e^2)^3}\\
& + J_4\,\frac{15R_M^4 n}{1024a^4\left(1-e^2\right)^4}\left(-63e^2\cos(4i-2\omega)-28e^2\cos(2(i-\omega))-28e^2\cos(2(i+\omega))\right.\\
& \quad -63e^2\cos(2(2i+\omega))+4\left(63e^2+52\right)\cos(2i)+7\left(27e^2+28\right)\cos(4i)-10e^2\cos(2\omega)\\
& \quad \left.+135e^2-14\cos(4i-2\omega)+8\cos(2(i-\omega))+8\cos(2(i+\omega))-14\cos(2(2i+\omega))+12\cos(2\omega)+108\right)\\
& + J_5\,\frac{15\mu R_M^5 n\sin\omega}{256a^5e\left(1-e^2\right)^5}\left(7e^2s_i\,c_i^2\left(e^2(-(15\cos(2i)+1))\cos(2\omega)-15\left(5e^2+8\right)\sin^2(i)+64e^2+96\right)\right. \quad (25)\\
& \quad -16\left(3e^2+4\right)e^2c_i\cot(i)+s_i\left(-21s_i^4\left(-30e^4-79e^2+6\left(2e^4+e^2\right)\cos(2\omega)-8\right)\right.\\
& \quad \left.\left.+112s_i^2\left(\left(2e^4+e^2\right)\cos(2\omega)-2\left(4e^4+10e^2+1\right)\right)+16\left(18e^4+41e^2+4\right)\right)\right)\\
& + J_6\,\frac{105R_M^6 n}{4096a^6\left(1-e^2\right)^6}\left(-\frac{1}{2}c_i^2\left(8\left(15e^4+40e^2+8\right)\left(33s_i^4+8\right)-3e^4\sin^2(i)(33\cos(2i)+7)\cos(4\omega)\right.\right.\\
& \quad -5e^2\left(e^2+2\right)\left(-12\cos(2i)+99\cos(4i)+41\right)\cos(2\omega)\Big)+33\sin^6(i)\left(\left(7e^2+4\right)e^2\cos(4\omega)\right.\\
& \quad -10\left(7e^4+22e^2+4\right)\cos(2\omega)+14\left(5e^4+20e^2+8\right)\Big)-6\sin^4(i)\left(5\left(7e^2+4\right)e^2\cos(4\omega)\right.\\
& \quad -80\left(7e^4+22e^2+4\right)\cos(2\omega)+126\left(5e^4+20e^2+8\right)\Big)-16\sin^2(i)\left(10\left(7e^4+22e^2+4\right)\cos(2\omega)\right.\\
& \quad \left.\left.\left.-21\left(5e^4+20e^2+8\right)\right)-2\left(-55e^4-40e^2+9\left(15e^4+40e^2+8\right)\cos(4i)+56\right)\right).
\end{aligned}
$$

$$
\begin{aligned}
\frac{de}{dt} = & -J_3\,\frac{3R_M^3 n\,e\,s_i\cos\omega(-4+5\sin^2 i)}{8a^3(1-e^2)^2} + J_4\,\frac{15R_M^4\,n\,e\,s_i^2(7\cos(2i)+5)\sin(2\omega)}{64a^4\left(1-e^2\right)^3}\\
& - J_5\,\frac{15R_M^5 n\,s_i\cos\omega}{2048a^5\left(1-e^2\right)^4}\left(-63e^2\cos(4i-2\omega)+28e^2\cos(2(i-\omega))+28e^2\cos(2(i+\omega))\right.\\
& \quad \left.-63e^2\cos(2(2i+\omega))+28\left(5e^2+8\right)\cos(2i)+21\left(9e^2+8\right)\cos(4i)+70e^2\cos(2\omega)+55e^2+120\right)\\
& - J_6\,\frac{105eR_M^6 n\,s_i^2}{8192a^6\left(1-e^2\right)^5}\left(12e^2s_i^2(11\cos(2i)+9)\sin(4\omega)+5\left(e^2+2\right)(60\cos(2i)+33\cos(4i)+35)\sin(2\omega)\right).
\end{aligned}
$$

– $\overline{C}_{22}$ term: $\langle\langle R_{C_{22}}\rangle\rangle$.

$$
\begin{aligned}
\frac{d\omega}{dt} &= -\frac{3}{2}\frac{n\,\overline{C}_{22}R_M^2\,\cos(2(\Omega-\gamma_M t))\left(5\,c_i^2-3\right)}{a^2\left(e^2-1\right)^2},\\
\frac{de}{dt} &= 0. \qquad (26)
\end{aligned}
$$

– Sun gravitational perturbation and solar radiation pressure: $\langle\langle R_{3b}\rangle\rangle+\langle\langle R_{SRP}\rangle\rangle$. These terms can be combined after double-averaging process: $(1-\beta)\langle\langle R_{3b}\rangle\rangle$.

$$\frac{d\omega}{dt} = (1-\beta)\Bigg[-\frac{3n_{\odot}^2\sqrt{1-e^2}}{4n\left(1-e_{\odot}^2\right)^{3/2}}\Big(4(\alpha_1^2+\alpha_2^2)-(\gamma_1^2+\gamma_2^2)-\frac{4}{3}\Big)$$
$$+\frac{3\,n_{\odot}^2\,\cot i}{4n\sqrt{1-e^2}\left(1-e_{\odot}^2\right)^{3/2}}\Big((1+4e^2)\Big(\alpha_1\frac{\partial\alpha_1}{\partial i}+\alpha_2\frac{\partial\alpha_2}{\partial i}\Big)+(1-e^2)\Big(\gamma_1\frac{\partial\gamma_1}{\partial i}+\gamma_2\frac{\partial\gamma_2}{\partial i}\Big)\Big)\Bigg],$$
$$\frac{de}{dt} = (1-\beta)\frac{15\,n_{\odot}^2\,e\,\sqrt{1-e^2}}{4n\left(1-e_{\odot}^2\right)^{3/2}}\Big(\alpha_1\gamma_1+\alpha_2\gamma_2\Big). \tag{27}$$

References

1. Abad, A., A., Elipe, A., Tresaco, E.: Analytical Model to Find Frozen Orbits for a Lunar Orbiter. Journal of Guidance, Control, and Dynamics, Vol. 32, No. 3, pp.888–898, (2009).
2. Battin, R. H.: An introduction to the mathematics and methods of astrodynamics. AIAA Educational Series. Published by American Institute of Aeronautics and Astronautics, Inc, (1999).
3. Broucke, R.A.: Long-Term Third-Body Effects via Double Averaging. Journal of Guidance, Control, and Dynamics. Vol. 26, No. 1, pp. 2732, (2003).
4. Carvalho, J. P. S., Vilhena de Moraes, R., Prado A. F. B. A.: Dynamics of artificial satellites around Europa. Mathematical Problems in Engineering. 2013, 7 pages, (2013).
5. Carvalho, J. P. S., Vilhena de Moraes, R., Prado A. F. B. A.: Some Orbital Characteristics of Lunar Artificial Satellites, Celestial Mechanics and Dynamical Astronomy. Vol. 108, pp. 371–388, (2010).
6. Celletti, A., Galeş, C., Pucacco, G., Rosengren, A. J.: Analytical development of the lunisolar disturbing function and the critical inclination secular resonance. Celestial Mechanics and Dynamical Astronomy. Vol. 127, pp. 259–283, (2017).
7. Danby, J. M. A.: Fundamentals of Celestial Mechanics, Willmann-Bell, Inc., Richmond, (1988).
8. Delsate, N., Robutel, P., Lemaître, A., Carletti, T.: Frozen orbits at high eccentricity and inclination: application to Mercury orbiter. Celestial Mechanics and Dynamical Astronomy. Vol. 108, pp. 275-300, (2010).
9. Elipe, A., Lara, M.: Frozen Orbits about the Moon. Journal of Guidance, Control, and Dynamics. Vol. 26, No. 2, pp. 238–243, (2003).
10. Fieseler, P. D.: A method for solar sailing in a low Earth orbit. Acta Astronautica. Vol. 43, No. 9-20, pp. 531–541, (1998).
11. Fu, B., Sperber, E., Eke, F.: Solar sail technology-A state of the art review. Progress in Aerospace Sciences. Vol. 86, pp. 1-19, (2016).
12. Giacaglia, G.E.O., Murphy J., Felsentreger, T.: A Semi-Analytic Theory for the Motion of a Lunar Satellite. Celestial Mechanics and Dynamical Astronomy. Vol. 3, pp. 3-66, (1970).
13. Imperi, L., Mariani M., Iess L.: BepiColombos geodesy and relativity experiments from an extended mission. Geophysical Research Abstracts Vol. 17, EGU2015-13332-1, (2015).
14. Jehn, R.: BepiColombo Mercury Cornerstone Consolidated Report on Mission Analysis, MAS Working Paper No. 525, BC-ESC-RP-05500, Issue 5.2, European Space Operations Centre, (2015).
15. Kaula, W. M.: Theory of satellite geodesy. Applications of satellites to geodesy. Waltham, Mass.: Blaisdell, (1966).
16. Lara, M., Deprit, A., Elipe, A.: Numerical continuation of frozen orbits for the zonal problem. Celestial Mechanics and Dynamical Astronomy, 62, pp. 167-181, (1995).
17. Lara, M., Palacián, J. F., Yanguas, P., Corral, C.: Analytical theory for spacecraft motion about Mercury. Acta Astronautica. Vol. 66, pp. 1022–1038, (2010).

18. Lidov, M. L. Yarskaya, M. V.: Integrable Cases in the Problem of the Evolution of a Satellite Orbit under the Joint Effect of an Outside Body and of the Noncentrality of the Planetary Field. Cosmic Research. 139-152, (1974).
19. Liu, X., Baoyin, H., and Ma, X.: Long-Term Perturbations Due to a Disturbing Body in Elliptic Inclined Orbit. Astrophysics Space Science, Vol. 339, No. 2, pp. 295304, (2012).
20. Ma, X., Li, J.: Artificial frozen orbits around Mercury. Astrophys Space Sciences. Vol. 348, pp. 345–365, (2013).
21. Margot, JL., Peale, S. J., Solomon, S. C., Hauck, S. A., Ghigo, F. D., Jurgens, R. F., Yseboodt, M., Giorgini, J. D., Padovan, S., Campbell, D. B.: Mercury's moment of inertia from spin and gravity data. Journal of Geophysical Research: Planets. Vol. 117, (2012).
22. Mazarico, E., Genova, A., Goossens, S.: The gravity field, orientation, and ephemeris of Mercury from MESSENGER observations after three years in orbit. Jounal of Geophys. Res. Planets. 119:2417-2436, (2014).
23. McInnes, C. R.: Solar Sailing: Technology, Dynamics and Mission Applications. Springer-Praxis Series in Space Science and Technology, Springer-Verlag, (1999).
24. Meyer, W. K., Buglia, J. J., Dsai, P. N.: Lifetimes of lunar satellite orbits. NASA STI/Recon Technical Report N-TP-3394 94. 27771, (1994).
25. Milani, A., Gronchi, G.: Theory of Orbit Determination. Cambridge University Press - Mathematics. 382 pages, (2010).
26. Noyelles, B., Frouard, J., Makarov, V., Efroimsky M.: Spin-orbit evolution of Mercury revisited. Icarus, Vol. 241, pp. 26-44, (2014).
27. Stark, A., Oberst, J., Hussmann, H.: Mercury's resonant rotation from secular orbital elements. Celestial Mechanics and Dynamical Astronomy. Vol. 123, pp. 263–277, (2015).
28. Tresaco, E., Elipe, A., Carvalho, J. P. S.: Frozen Orbits for a Solar Sail Around Mercury. Journal of Guidance, Control, and Dynamics. Vol. 39, No. 7, pp. 1659-1666, (2016).
29. Vallado, D. A., McClain, W. D.: Fundamentals of Astrodynamics and Applications. New York: McGraw-Hill Companies, Inc. (1997).
30. Verma, A. K., Margot, J. L.: Mercury's gravity, tides, and spin from MESSENGER radio science data. J. Geophys. Res. Planets. Vol. 121, (2016).
31. Sampaio, J.C., Neto, A.G.S., Fernandes, S.S., Vilhena de Moraes, R.: M.O. Terra Artificial satellites orbits in 2:1 resonance: GPS constellation. Acta Astronautica. Vol. 81, pp. 623634, (2012).
32. Winglee, R.M., Slough, J., Ziemba, T., Goodson, A.: Mini-Magnetospheric Plasma Propulsion: Tapping the energy of the solar wind for spacecraft propulsion. J. Geophys. Res. Vol. 105, No. A9, pp. 21.067-21.077, (2000).